Separation and Purification Technology 375 (2025) 133807

Contents lists available at ScienceDirect

Separation and Purification Technology

journal homepage: www.elsevier.com/locate/seppur

Iron nanoparticles embedded porous chitosan for antimony removal: exceptional adsorption capacity, cations resistance and environmental recyclability

Hongjie Wu [a], Xiaoyu Jia [b,c,*], David Hermann Lamparelli [d], Dirong Gong [a,*], Antonio Buonerba [d,*]

[a] Faculty of Materials Science and Chemical Engineering, Ningbo University, Ningbo 315211, PR China
[b] Key Laboratory of Urban Environment and Health, Institute of Urban Environment, Chinese Academy of Sciences, No.1799, Jimei Road, Xiamen, Fujian 361021, PR China
[c] ZheJiang Key Laboratory of Urban Environmental Processes and Pollution Control, Ningbo Observation and Research Station, Institute of Urban Environment, Chinese Academy of Sciences, Ningbo 315830, PR China
[d] Department of Chemistry and Biology "Adolfo Zambelli", University of Salerno, Via Giovanni Paolo II, 132, 84084 Fisciano, SA, Italy

ARTICLE INFO

Keywords:
Iron nanoparticles
Well-dispensed
Sustainable
Anti-interference
Antimony removal

ABSTRACT

Antimony (Sb) is an important element applied in many industries, and its uncontrolled discharge into the environment has seriously impacted the ecological systems. Bulk adsorbents such as metal oxides, metal nanoparticles, metal salts, and organic-metal frameworks were used with a low atom utility efficiency for Sb recovery. In this work, zero-valent iron nanoparticles (Fe(0)) were uniformly embedded on bio-derived porous chitosan hydrogel via an in-situ reduction procedure. The as-prepared materials improve Sb adsorption uptake up to 175.89 $mg_{Sb}{\cdot}g_{Ad}^{-1}$ or 2240.73 $mg_{Sb}{\cdot}g_{Fe}^{-1}$, far more than those of the previously reported bulk iron analogs, highlighting the significant role of supporting strategy in enhancing Fe-atom efficiency. The variations of the performances with the experimental parameters, including contacting time, initial Sb amount, adsorbent doping, temperature, coexisting cations, pH, as well as cyclic removal performance, were fully investigated. The materials exhibit a robust resistance to high concentrations of interfering cations Co^{2+}, Ni^{2+}, Cu^{2+}, As^{3+}, Sr^{+}, and Cd^{2+} with a significant adsorption constant ratio $K_{Sb/M}$ up to 214–4548. The resilience to performance fatigue is highlighted by five consecutive adsorption–desorption cycles retaining over 80.9 % of the original efficiency, supporting circular economy. The adsorption pathway, including oxidation–reduction and ionic affinity, has been probed, and XPS corroborates the findings. The developed fabrication strategy shows fundamental guidance for constructing highly efficient eco-friendly materials for treating Sb-polluted water and can be extended to other hazardous substances.

1. Introduction

Antimony is an important element in the production of polyester, electrodes, flame retardants, as well as in energy storage and automotive applications [1]. The annual production of Sb exceeds 150 Mtons [2]. However, the pollution caused by emissions from textile manufacturing, mining, metallurgy, vehicular emissions, printing, and dyeing poses significant risk on the human environment [3–5], particularly the aquatic environment [1]. The antimony concentration in some sewage reaches as high as 100–7000 $mg{\cdot}L^{-1}$ [6], far beyond the conventional safety standard of 5 ~ 100 $\mu g{\cdot}L^{-1}$ [7]. Therefore, strict control of antimony contaminants in water is imperative [8].

Antimony ions can enter the human body through the skin, inhalation and ingestion [9], interfering with metabolism and finally leading to cell death. Antimony can also damage the central nervous system. The biological toxicity of antimony varies depending on the oxidation state, physical form, and the way of ingestion. Antimony has two oxidation states, Sb(III) and Sb(V) [7] in the natural environment [10]. Generally, Sb(III) exhibits far more toxicity than Sb(V); therefore, its impact on the environment. The form of Sb(III) is pH-dependent. As the pH changes from acidic to basic, the cationic $Sb(OH)_2^+$ is converted to the electrically neutral H_3SbO_3 and $Sb(OH)_3$ species and finally to the anionic species

* Corresponding authors.
E-mail addresses: xyjia@iue.ac.cn (X. Jia), gongdirong@nbu.edu.cn (D. Gong), abuonerba@unisa.it (A. Buonerba).

https://doi.org/10.1016/j.seppur.2025.133807
Received 3 April 2025; Received in revised form 23 May 2025; Accepted 28 May 2025
Available online 30 May 2025
1383-5866/© 2025 The Author(s). Published by Elsevier B.V. This is an open access article under the CC BY license (http://creativecommons.org/licenses/by/4.0/).

$H_2SbO_3^-$, $Sb(OH)_4^-$. Similarly, Sb(V) transforms from SbO_2^+ to the neutral $Sb(OH)_5$ species and finally to the anionic $Sb(OH)_6^-$ species [11].

Recently, researchers have developed a variety of strategies for treating antimony contaminants, including ion exchange [12], electrochemical methods [13], membrane separation [14], and adsorption [15], where the latter has been considered to be one of the most efficient with the advantages of cost-effectiveness, abundant choice of the materials and variable options of design [16]. It is also believed that the choice of materials is inextricably linked to removal performances. Recent years have witnessed an increasing number of functional materials innovated for antimony removal, including metal-based, particularly iron materials [17], carbon-based composites [18], MOF [19], and organic–inorganic hybrids [15].

Zhang et al., developed γ-Fe_2O_3, γ-FeOOH and Fe_3O_4-based materials to improve the antimony removal performance [20]. Mittal et al., investigated the performances of Sb(III) removal by Fe_3O_4 [21]. In these cases, it has been revealed that the antimony oxygen anions are attracted to the protonated surface hydroxyl functional groups and form complexes via the Fe-O-Sb moiety. Zero-valent nano-iron (Fe(0)) has recently been widely used for antimony treatment due to its large surface area and strong reducing capability [22]. The results show that the iron oxides on the surface of the Fe(0) core can provide additional active sites to host antimony and facilitate affinity with Fe(0) [23]. The number of activated adsorption sites can also be increased by applying an external weak magnetic field, which causes a change in the paramagnetic gradient at the Fe(0) surface [24], thus accelerating the mass transfer at the metal interface [25]. Moreover, the surface of the nanoparticles can be modified with surfactants to avoid oxidation and aggregation of particles [3–5]. In general, an oxygen-rich cellulose, lignin and sodium alginate [26,27] have been proven to have such a function [3–5]. Chitosan (CS), a sustainable substance, has abundant hydroxyl and amino groups which is also of high potentials for modification [28–30]. Due to unique attraction to the metal ions, chitosan has been applied in environment treatments, particularly to separate metal elements from the aqueous environment. Chitosan was also found to compound with iron oxides in a few recent examples [31,32]. Zeng et al., found that iron/CS composites were able to accelerate chelation and electrostatic attraction with Sb(III), with adsorption of 139 $mg{\cdot}g^{-1}$ [15]. Lapo et al., prepared chitosan-supported Fe(III) beads and found that α-FeO(OH) is the main active species for attracting the Sb species with a resulting adsorption capacity can be 626 $mg_{Sb}{\cdot}g_{Fe}^{-1}$ [33]. Therefore, combining CS and iron active centers presents a promising approach for developing efficient materials to treat the Sb-contaminated water media.

This study reports a novel composite of Fe(0) nanoparticles encapsulated in chitosan porous materials prepared from the hydrogel via the freeze-drying method and its remarkable removing performances of Sb. The purposes of this study are: 1) the fabrication of a novel type of well-dispersed nano-sized Fe(0) absorbent suitable for Sb treatment via compounding with porous CS hydrogel; 2) the evaluation of the overall performances by varying the experimental conditions, *i.e.*, adsorbent and Sb feeding amount, contacting time, pH, competing cations, as well as the cyclic adsorption–desorption; 3) to reveal the contribution of iron species behind the removal performances of Sb.

The eco-friendly materials significantly improve Sb adsorption uptake up to 175.89 $mg_{Sb}{\cdot}g_{Ad}^{-1}$ or 2240.73 $mg_{Sb}{\cdot}g_{Fe}^{-1}$, recording one of the best performed adsorbents. Moreover, the materials showed a very strong preference for Sb adsorption with competing constants $K_{Sb/M}$ up to 214–4548 (co-existing cations M: Co^{2+}, Ni^{2+}, Cu^{2+}, As^{3+}, Sr^{+}, and Cd^{2+}). And, cyclic use of the materials is also demonstrated retaining more than 80.9 % pristine capacity. The developed nano-sized Fe(0) fabrication strategy shows fundamental guidance for constructing advanced materials for addressing the aquatic Sb element and beyond.

2. Experimental

2.1. Materials

Acetic acid (99.7 %), iron dichloride tetrahydrate, sodium borohydride (98 %), chitosan (75 %), methanol (analytic grade), sodium hydroxide (99.5 %), and nitric acid solution (HNO_3, 65.0 wt%) were purchased from commercially available sources. Deionized water was made in lab. Tap water was supplied by Ningbo Tapwater Company. Aqueous stock of Sb (III, V, 1000 $mg{\cdot}L^{-1}$) solutions and those mixed with cationic ions (Cu^{2+}, Cd^{2+}, Co^{2+}, Ni^{2+}, Sr^{1+}, $Zn^{2+,}$ and As^{3+}) were available from the National Standard Material Center of China. Diluted Sb(III + V) aqueous solutions were freshly prepared in deionized water, and the pH was regulated with a standard 0.01 M NaOH or HNO_3 aqueous solution.

2.2. Synthesis of Fe(0)-CS nanocomposites

A chitosan (0.8 g) viscous solution in acetic acid (80 mL) was compounded with $FeCl_2{\cdot}4H_2O$ (0.23 g) portions under vigorous stirring. The addition of $NaBH_4$ (0.05 g) was then immediately followed in portions [34]. The resulting dark viscous suspension was then poured into a 3.0 wt% sodium hydroxide solution using a syringe under a nitrogen stream, obtaining dark brown hydrogel microspheres (Scheme 1). The beads were then freeze-dried for 12 h. The prepared materials were stored under a nitrogen atmosphere.

2.3. Materials' characterization and instrumentations

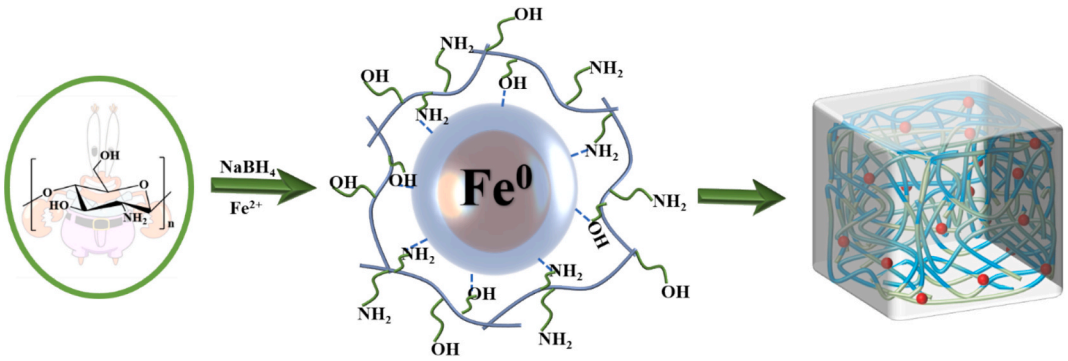
The Fourier transform infrared (FT-IR) spectra were recorded on an 8400S FT-IR spectrophotometer from Shimadzu (Japan). The morphologies of the materials were investigated by scanning electron microscopy (SEM) with a JSM-6010LA microscope from JEOL (Japan). Elemental compositions were analyzed by an SU8220 SEM microscope (Japan) equipped with an energy dispersive spectrometer (EDS) module from Oxford (UK). The surface elemental percentage and oxidation state of iron elements were analyzed by Thermo Scientific K-Alpha$^+$ and calibrated with respect to C1s peak at 284.8 eV. Thermogravimetric analyses (TGA) were performed on a Perkin Elmer 8000 analyzer in the 50–800 °C with a ramp of 10 °C/min. The inner pores' specific surface area and size were measured by the Brunauer-Emmett-Teller (BET) method at 77 K using an Autosorb IQ analyzer. Sb concentrations were determined by Inductively Coupled Plasma-Mass Spectrometry (ICP-MS) with a Thermo Fisher Scientific (USA) analyzer. Dynamic Laser Scattering (D.L.S) for analysis of particles size of Fe (0) was carried out using Malvern Zetasizer Nano ZS90.

2.4. Antimony adsorption tests with Fe(0)-CS

Adsorption studies were handled in a fume hood under safety guards, and the produced wastes were deposited in a dedicated container, strictly following the Material Safety Data Sheet (MSDS) for Sb-containing substances. Batch adsorption experiments were performed in at least three independent batches, and the data were reported as mean values ± standard deviations (error bar). The adsorption amount was calculated by subtracting the residual ion concentration in the solution.

2.5. Kinetic studies of Sb adsorption with Fe(0)-CS

The adsorption kinetics were investigated individually using different dosages of adsorbent (2, 4, 6, 8, 11, and 12 $g{\cdot}L^{-1}$), and the capacity with respect to contacting time was calculated. Typically, Fe (0)-CS (100 mg) was placed in a sealed flask containing Sb aqueous solution (150 mL, 500 $mg{\cdot}L^{-1}$), and the adsorption was performed at 30°C, pH of 6.0 ± 0.1 and a stirring rate of 200 rpm. Aliquots (0.5 mL)



Scheme 1. Synthetic route of Fe(0)-CS composite.

were then sampled at the desired time (t) using a syringe, and the solutions were filtered with membranes of 0.22 μm pore size. The residue Sb (C_t) in the resultant solutions was quantitatively determined by ICP-MS, and the time-dependent correlation was obtained. A kinetics study was also performed using neat cellulose for comparison.

The adsorption capacity (Q_t) was determined using the following equation:

$$Q_t = \frac{(C_0 - C_t)V}{m} \quad (1)$$

where: Q_t (mg·g^{-1}) is capacity of Sb adsorbed at a predetermined time t(min); C_O(mg·L^{-1}) and C_t(mg·L^{-1}) are the beginning (0 min) and sampling (t min) concentrations of Sb, respectively; V (L) refers to volume of aqueous sample at the beginning (0 min) and m (g) refers to dry weight of the adsorbent employed.

2.6. Adsorption isotherm studies of Sb with Fe(0)-CS

The adsorption isotherms were followed by conducting separate experiments at different Sb feeding concentrations. Each aqueous Sb solution with concentrations of 1, 50, 100, 200, 300, and 500 mg·L^{-1} in a sealed flask was compounded with the absorbent (100 mg). The adsorption was conducted under the same conditions as noted in 1.4.1. After the end of each run, the absorbent was separated, and the remaining Sb was determined.

2.7. Study of the effect of pH on Sb removal with Fe(0)-CS

Adsorptions were performed separately in a solution containing 10 mg·L^{-1} of Sb at different pHs of 3.0–11.0 using 15 mg of absorbent under the above experimental conditions.

2.8. Cation effect on Sb removal with Fe(0)-CS in tap water

Adsorption was carried out in tap water containing Sb (128.0 mg·L^{-1}) and competing ions Cu^{2+} (47.9 mg·L^{-1}), Cd^{2+} (49.8 mg·L^{-1}), Co^{2+} (51.1 mg·L^{-1}), Ni^{2+} (50.6 mg·L^{-1}), Sr^{1+} (49.5 mg·L^{-1}), Zn^{2+} (37.3 mg·L^{-1}) and As^{3+} (38.4 mg·L^{-1}) by the use of 100 mg absorbent under the other experimental conditions as the same as described above. The residual concentration of each ion was determined after reaching the equilibrium.

2.9. Optimization of adsorbent amount in Sb removal with Fe(0)-CS

Adsorption was separately performed in a 150 mL solution with an initial concentration of 1000 ppm of Sb using 20, 40, 60, 80, 100 and 120 mg of Fe(0)-CS under the experimental conditions above described. The Sb adsorption amount was determined by subtracting the remaining Sb concentration in the solution.

2.10. Adsorbent regeneration and re-use in Sb removal with Fe(0)-CS

The Sb desorption was performed by treatment with 25 mL of 0.5 M NaOH solution at 25 °C for 12 h. The recovered Sb in the solution was determined by ICP-MS to evaluate the desorption efficiency. The regenerated beads were washed with deionized water and methanol at pH 7 and then dried in a vacuum under liquid nitrogen for the next adsorption–desorption cycle under the same experimental conditions.

2.11. Adsorption thermodynamic investigations on Sb removal with Fe (0)- CS

Adsorption was individually conducted using 120 mg of Fe(0)-CS in 150 mL of 500 ppm solution of Sb at 30, 40, 50, 60 and 70 °C until adsorption was saturated. Capacity calculations and analyses were performed as above described.

3. Results and Discussion

3.1. Synthesis and characterization of Fe(0)-CS

Fig. 1a and b reports the FT-IR spectra of CS and the corresponding Fe(0)-CS composites before and after adsorption. In the FT-IR spectra of Fe(0)-CS, a significant decrease in intensity of the amino bands at wavenumber of 3340 cm^{-1} and 1586 cm^{-1} [35] is observed after compounding CS with Fe(0) [36], and completely disappears after adsorption due to affinity with Sb. The adsorption band –OH shift from 3565 cm^{-1} to 3519 cm^{-1} is also visible. These results suggest successfully fabricating CS and Fe(0) particles through binding with amines and hydroxyl donors [37–38]. The attenuation of the two characteristic absorption bands at 1037 cm^{-1} and 512 cm^{-1} from the chitosan correspond to C–O and C–N stretching vibrations, respectively [39] was also observed after coordination of these moieties to the iron nanoparticles. The C–O intensity is also declined probably resulted from the O–Sb interaction.

The thermal stability of Fe(0)-CS was verified by thermogravimetric (TGA) analysis. As shown in Fig. 1b, Fe(0)-CS degradation follows a three-stage pattern compared to the single-state one of the pristine CS. The first stage starts at ≈100 °C and ends at 170 °C, with a weight loss of 11.0 wt% that can be ascribed to the release of water. The second stage corresponds to a partial decomposition of the main chain of CS via oxidative degradation with a weight loss of about 60.0 wt% before 300 °C [40]. During this stage, forming the char layer covering the surface of the materials is possible, slowing down further decompositions. This causes the third stage to occur at a beginning temperature of 310 °C up to 410 °C. Complete degradation of organic matter is observed at 475 °C. The final residue is assumed to be iron oxide, accounting for 2.0 wt%.

XRD analysis was employed to gain information on the inner structure of Fe(0)-CS, and the corresponding diffractogram is reported in

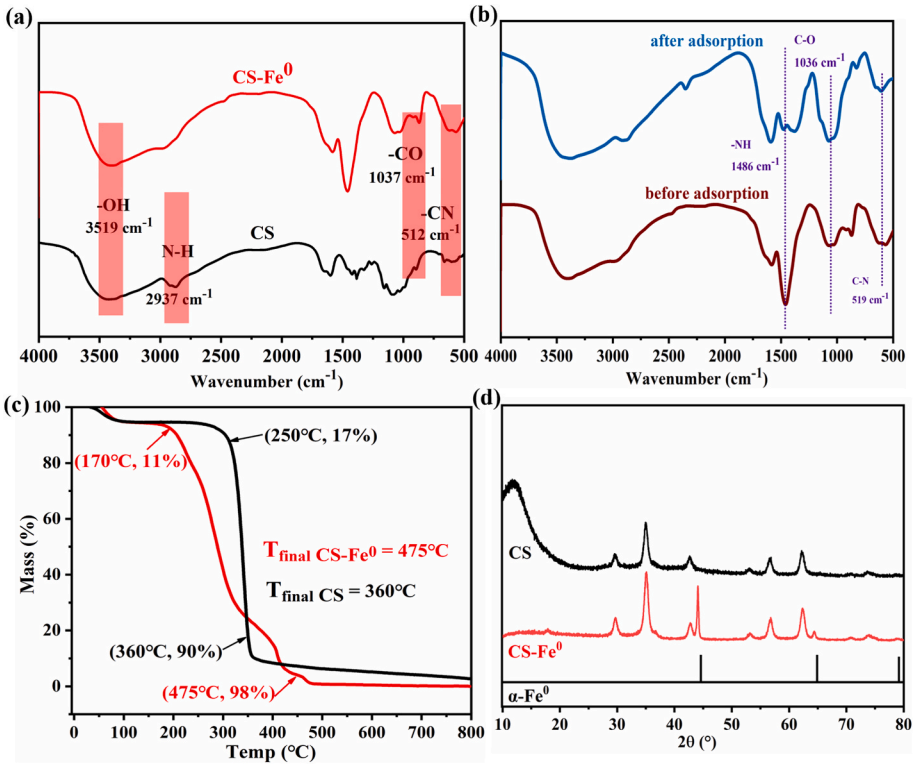


Fig. 1. The FT-IR spectra (a, of pristine CS and Fe(0)-CS; b, before and after the adsorption), TGA profiles (c), and X-ray diffraction patterns (d) of pristine CS and Fe (0)-CS.

Fig. 1c. It is possible to observe that the diagnostics reflexes for the crystalline Fe(0) particles [41–42] at 2θ of 44.6°, 65°, and 79° are present in the Fe(0)-CS composite, together with the diagnostic signal for the crystalline CS at 29.9° and 35.8° [43]. The broad signals found for the Fe(0) reflexes indicate the formation of small nanometric particles. This information suggests that zero-valent iron nanoparticles are successfully fabricated into the chitosan matrix [10].

The inner sections of Fe(0)-CS were obtained by fracture after immersion in liquid nitrogen for 20 min and sputter-coating with metal gold before scanning electron microscopy (SEM) analysis. The material's morphology was then investigated by scanning electron microscope coupled with energy-dispersive X-ray spectroscopy, and the morphology was shown in Fig. 2b. By magnification in Fig. 2b and c, a microporous structure was observed with pore dimensions of several hundred

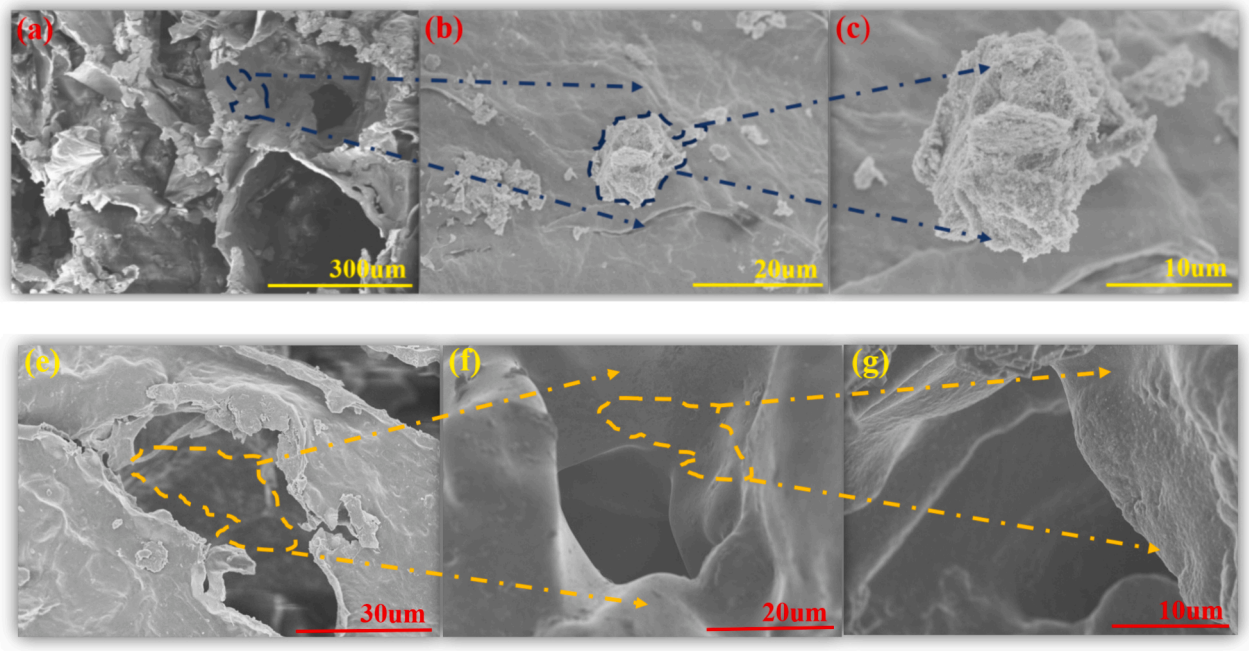


Fig. 2. SEM micrographs of Fe(0)-CS under different magnifications.

micrometers in diameter. The pores are penetrated to create efficient mass transfer channels, and such a hollow three-dimensional (3-D) structure offers the possibility of a large mass transfer and contacting surface when exposed to a targeted pollutant [44]. The energy dispersive X-ray spectroscopy shows areas composed of C, O, and N. Clear iron element spots with uniform distribution could be seen in the elemental maps reported in Fig. 3a, and the actual composition determined by ICP-MS of 7.8 wt% was closely matched with the loaded amount of 8.1 wt%. The presence of Fe(0) can be verified by the XPS spectrum, and the exact component will be discussed later in the mechanistic subsection (see section 3.6). The particles size was estimated by the D.L.S and the average value is 136.6 nm (Fig. 3b).

N_2 adsorption–desorption isotherms were studied to further gain information on the inner pore surface and structures. The hysteresis loops in the isotherms found were characteristic for type I materials, showing the typical features of microporous materials as shown in Fig. 4a. The specific surface area determined was 28.5 $m^2 \cdot g^{-1}$. The pore diameter ranges from 2.5 to 35 nm, and the average value was calculated to be 19.0 nm. Therefore, such a large surface and unique micro-size structure is potentially helpful to mass transfer and ion retention (*vide infra*). After saturation with Sb, the specific surface decreased to 10.719 $m^2 \cdot g^{-1}$, and the average pore size was estimated to be 10.832 nm (Fig. 4b).

3.2. Kinetics and isotherms study on Sb adsorption

Fe(0)-CS uptake behavior in the solutions containing Sb with various dosages of adsorbents has been investigated. The flask, equipped with a shaker, was fed with an initial concentration of 500 $mg \cdot L^{-1}$ of the targeted analyte. Adsorption was initiated (t_0) by adding Fe(0)-CS to the working solution at 30 °C at a stirring rate of 180 rpm. After a given time (t), aliquots of solution were extracted and filtered using nylon syringe filters with a 0.22-μm pore size, and the Sb concentration was determined by an ICP-MS [45]. The adsorption capacity Q_t ($mg \cdot g^{-1}$) was calculated from Equation (1).

The uptake kinetics ($Q_t \sim t$) of Sb ion and the analyses were depicted in Fig. 5. The curves from different absorbent dosages in Fig. 5a illustrate adsorption rate using Fe(0)-CS is rapid and very efficient at the initial stage due to the high affinity of the material for dissolved Sb ions [46].

The efficiency reaches a plateau at initial dosages of 11 and 12 $g \cdot L^{-1}$. In the identified condition, the adsorption capacity Q_t reaches 52.79 $mg \cdot g_{Ad}^{-1}$ within 20 min, and the amount increases to 115.89 $mg \cdot g_{Ad}^{-1}$ within 60 min for Sb. Beyond that point, the adsorption undergoes at a steady stage, and after approximately 600 min, equilibrium is established and a final capacity up to 175.89 $mg_{Sb} \cdot g_{Ad}^{-1}$, exceeding most of the systems ever reported. This significant achievement highlights the supporting strategy remarkably enhances the iron atom utilization. A much lower equilibrium capacity below 34.5 $mg \cdot g^{-1}$ as shown in Fig. 5 (c) at a relatively sluggish rate (in 600 min) implies the role of sole CS is minor.

The kinetic data were simulated using the first-order model (Eq. (2)), second-order models (Eq. (3)), and intraparticle diffusion (Eq. (4)).

$$\lg(Q_e - Q_t) = \lg Q_e - k_1 t \quad (2)$$

$$\frac{t}{Q_t} = \frac{1}{k_2 Q_e^2} + \frac{t}{Q_e} \quad (3)$$

$$Q_t = kt^{0.5} + C \quad (4)$$

where k_1 ($g \cdot mg^{-1} \cdot min^{-1}$) and k_2 ($g \cdot mg^{-1} \cdot min^{-1}$) are the rate constants of pseudo-first-order, pseudo-second-order, respectively; Q_e ($mg \cdot g^{-1}$) and Q_t ($mg \cdot g^{-1}$) are the concentrations of Sb adsorbed at equilibrium time and time of t min, respectively; k ($mg \cdot g^{-1} \cdot min^{0.5}$) is the rate constants of intra-particle diffusion model; C ($mg \cdot g^{-1}$) is the intercept which can reflect the boundary layer thickness.

All models show a linear fitting line of the kinetic features. Considering a higher correlation coefficient of 0.999 for Sb and 0.98 for Sb-CS, as illustrated in Fig. 5(c), both processes are better fitted to a proposed second-order model by nonlinear fitting [47]. This indicates that the adsorption rates of Sb are dominated by chemisorption, and the number of active sites determines the removal capability. Accordingly, the corresponding adsorption rate constant, k, and theoretical equilibrium adsorption capacity, $Q_{e,cal}$, were determined and reported in Table 1. The adsorption capacity $Q_{e,\,cal}$ of Sb was calculated to be 117.65 $mg \cdot g^{-1}$ following in the experimental range (90.3–175.1 $mg \cdot g^{-1}$), and a better fitting value 22.7 $mg \cdot g^{-1}$ for Sb-CS was obtained [48].

Fig. 5d shows the fitting results using the internal diffusion model, where both adsorptions are composed of three stages representing three successive steps: surface diffusion, internal diffusion, and adsorption equilibrium [49]. The first stage corresponds to the ion diffusion from the bulk solution to the surface of Fe(0)-CS, and the high adsorption rate constant up to 7.13 $g \cdot mg^{-1} \cdot min^{-1/2}$ for Sb in this stage is attributed to the efficient mass transfer and the large surface of the adsorbent [50]. The fitted straight line does not extrapolate to the origin point, indicating that intra-particle diffusion is not the only rate-limiting step, consistent with the conclusion of the quasi-secondary kinetic fitting described above. In the second stage, diffusion of ions from the adsorbent's surface into the adsorbent's internal pores is presumed. The rate constants were calculated to be 0.81 $mg \cdot g^{-1} \cdot min^{-1/2}$, which is mainly affected by the nature of the active sites of the adsorbent. Finally, the adsorption reaches a stable stage, and a lower rate constant of 1.14 $mg \cdot g^{-1} \cdot min^{-1/2}$ is obtained [51]. The adsorption of Sb-CS undergoes a much slower rate.

The adsorption isotherm study was implemented under a dosage of

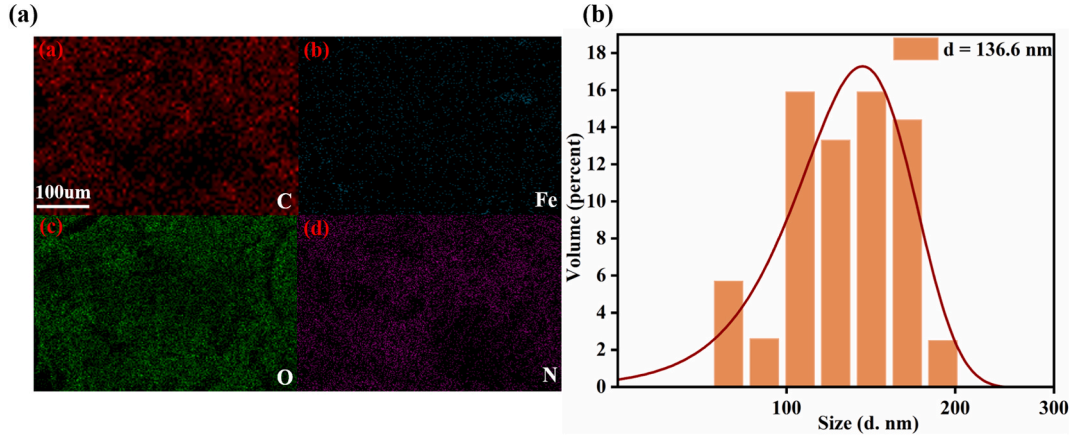


Fig. 3. Elemental distribution in Fe(0)-CS of C, O, N and Fe by SEM-EDX (a) and the Fe(0) size distribution by D.L.S (b).

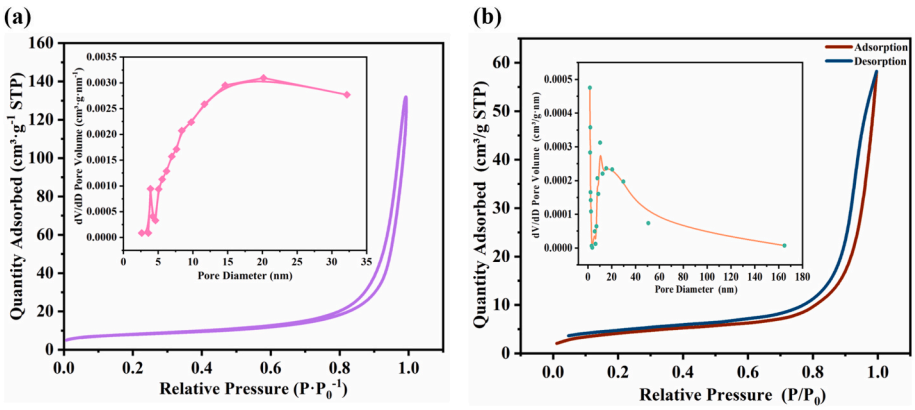


Fig. 4. BET curves for Fe(0)-CS before (a) and after (b) the Sb adsorption.

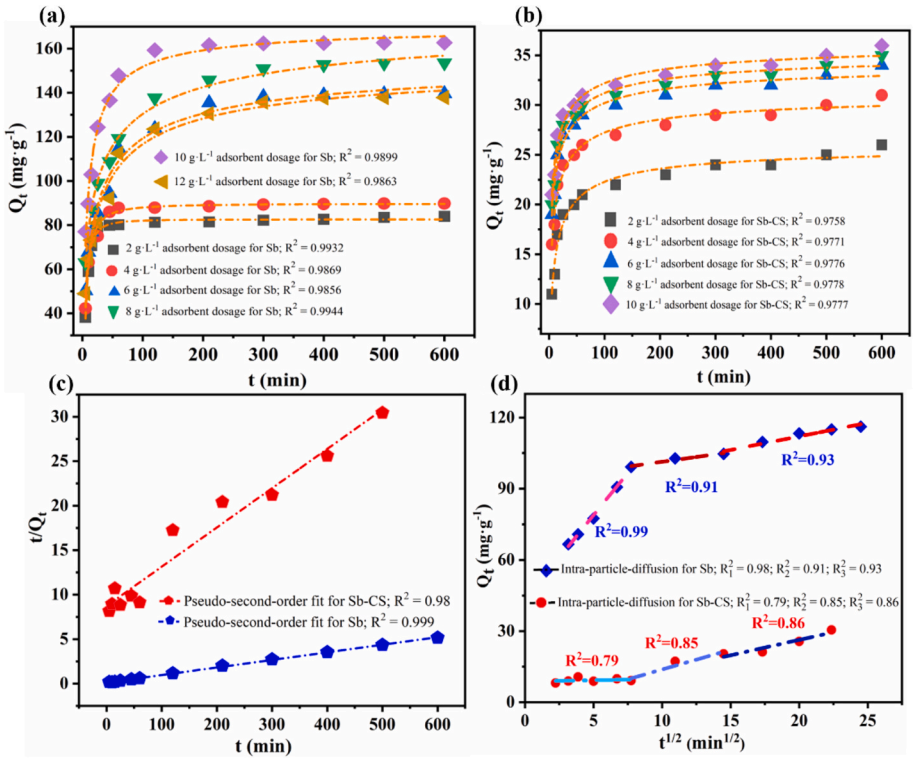


Fig. 5. (a) Adsorption capacities of Sb onto Fe(0)-CS as a function of time and fitting to pseudo-first-order kinetic model; (b) Adsorption capacities of Sb onto CS as a function of time and fitting to pseudo-first-order kinetic model; (c) fitting to pseudo-second-order kinetic model; and (d) fitting to intra-particle-diffusion model.

Table 1
Summarized fitting parameters for pseudo-first-order, pseudo-second-order, and intra-particle diffusion kinetic models.

	Pseudo-first order			Pseudo-second order			Intra-particle diffusion		
	k_1 (min^{-1})	$Q_{e,cal}$ ($mg{\cdot}g^{-1}$)	R^2	k_2 ($g{\cdot}mg^{-1}{\cdot}min^{-1}$)	Qe (cal/$mg{\cdot}g^{-1}$)	R^2	k_1; k_2; k_3 ($g{\cdot}mg^{-1}{\cdot}min^{-1/2}$)	C_1; C_2; C_3 ($mg{\cdot}g^{-1}$)	R^2
Sb-Fe(0)-CS	$6.91{\bullet}10^{-3}$	46.7	0.92	$5.87{\bullet}10^{-4}$	117.7	0.999	7.13; 0.81; 1.14	43.22; 93.26; 89.20	0.99, 0.91, 0.93
Sb-CS	$3.68{\bullet}10^{-3}$	22.9	0.95	$2.22{\bullet}10^{-4}$	22.7	0.98	0.12; 1.66; 1.29	8.70; 2.79; 0.36	0.79, 0.85, 0.86

100 mg of adsorbent in 120 ml of aqueous solution with varied Sb concentrations (1, 20, 50, 100, 300, and 1500 $mg{\cdot}L^{-1}$). The adsorption capacity was then calculated, and the fittings using Freundlich, Langmuir, and Temkin models were then carried out to estimate the adsorption and surface properties according to the following equations [52]:

$$\frac{C_e}{Q_e} = \frac{C_e}{Q_m} + \frac{1}{Q_m K_L} \tag{5}$$

$$\log Q_e = \log K_F + \frac{1}{n}\log C_e \tag{6}$$

$$Q_e = (\frac{RT}{b})\ln(K_T C_e) \quad (7)$$

where: k_L (L·min^{-1}), k_F (L·min^{-1}), and K_T (L·g^{-1}) are the fitting constants of Freundlich, Langmuir and Temkin models, respectively; Q_e (mg·g^{-1}) and Q_m (mg·g^{-1}) are the equilibrium and the theoretic maximal concentration of Sb adsorbed, respectively; C_e (mg·g^{-1}) is the equilibrium concentration and, finally, b refers to the order number of adsorption.

The adsorption fitting curves were given in Fig. 6 and the theoretical adsorption capacity Q_{eCal} and the adsorption constant k were presented in Table 2. The isotherm model was fitted by Langmuir method (Fig. 6a), and the maximum adsorption capacity of Sb obtained is up to 903.1 mg·g^{-1} with a high correlation coefficient R^2 equal to 0.988, so the isotherm model of the adsorption of Sb adsorbent spheres is better conformed with the Langmuir model. The Freundlich model was then fitted to the adsorption, and it was found that the correlation coefficient $R^2 = 0.954$ and the maximum adsorption capacity was calculated to be 769.7 mg·g^{-1} (Fig. 6a), thus the adsorption behavior of Sb in aqueous solutions with different concentrations of Sb is more in line with the Langmuir model. This suggests that the adsorption by adsorbent spheres is monolayer adsorption rather than multilayer adsorption. The fitting correlation coefficient R^2 equal to 0.88 using the Temkin model (Fig. 6b) is remarkably lower than 0.988 calculated from the Freundlich model, and the degree of conformity is less than that of the Langmuir model [53].

Langmuir fitting of the isotherm model for Sb-CS adsorption is also compared, and the calculated maximum adsorption capacity is 76.2 mg·g^{-1} with a correlation coefficient R^2 of 0.98, which deviates far from the actual value obtained experimentally. The Freundlich model was applied, and the correlation coefficient R^2 determined was 0.997, and the maximum adsorption capacity was 31.6 mg·g^{-1}, in accordance with the experimental one. Thus, the adsorption is more in accordance with the Freundlich model. This suggests that adsorption is multilayer rather than monolayer adsorption [54]. The calculated 1/n is 0.884, which is in the range of 0–1, indicating that the adsorption is a positive and favorable process. The fitted correlation coefficient R^2 using Temkin's model is 0.65, smaller than 0.99 from Freundlich's model, and the degree of conformity is less than that of Freundlich's model [55].

3.3. Sb adsorption thermodynamics in Fe(0)-CS

The adsorption kinetics and thermodynamics were carried out by adding 100 mg of adsorbent to 150 mL of 500 mg·L^{-1} aqueous Sb solution at the temperatures of 30, 40, 50, 60, and 70 °C, and each equilibrium adsorption capacity was calculated with Equation (1). The adsorption capacity Q_e is monotonously increased with the temperature (Fig. 7a), and the corresponding data are reported in Table 3. The values of Gibbs free energy change (ΔG) at each temperature were calculated and provided in Table 3: the negative values indicate that the adsorption is spontaneous and thermally feasible, highlighting the porous structure owing advantages to ion transfer and affinity with the adsorbent. The decreased trend demonstrated that the diffusion of ions out of the surface is more favored at the increasing of the temperature [56].

K_c and lnK_c were determined with the following equations:

$$K_c = \frac{Q_e}{C_e} \quad (8)$$

$$lnK_c = \frac{\Delta H}{RT} - \frac{\Delta S}{R} \quad (9)$$

where Q_e (mg·g^{-1}) is the concentration of adsorbed Tl at equilibrium, K_c (mL·g^{-1}) is the distribution coefficient, R (8.314 J·mol^{-1}·K) is the universal gas constant, and T (K) is the absolute temperature.

The relationship between 1000/T and lnK_c was depicted in Fig. 7b, and a good linearity was obtained with a fitting coefficient R^2 of 0.99. Thus, the enthalpy ΔH and entropy ΔS were estimated to be 95.9 kJ·mol^{-1} and 42.8 J·mol^{-1}·K^{-1}, respectively, using Eq. (9). The positive value of ΔH for the adsorption process indicates that the adsorption is a heat-absorbing process, verifying that a higher temperature favors the adsorption. The positive value of ΔS suggests that the process increases the disorder at the solid/liquid interface on the surface of the adsorbate spheres [57]. The coordination of Sb to the adsorber probably releases water molecules, thus increasing the entropy values.

3.4. Fe(0)-CS adsorbent regeneration and re-use

To evaluate the reusability, the Sb saturated materials were placed at 0.5 mol·L^{-1} NaOH aqueous solution for 12 h at 20 °C to recover the adsorbed Sb and restore the adsorbent. The detached Sb concentration was determined by ICP-MS, and ultimately, removal of as-adsorbed Sb was reached. The resultant beads were then washed with water and rinsed with methanol carefully under a nitrogen atmosphere and vacuum freezing-dry to afford the recovered adsorbent for the next cycle. Throughout five consecutive cycles of adsorption–desorption under the same conditions, a steady adsorption efficiency of more than 80.9 % could be obtained (Fig. 8) under feeding amount of 20.2–21.5 μg·L^{-1} of Sb, which indicates that the materials can be recycled for several times and its chemical and physico-mechanical properties are not damaged to a large extent [52]. The residual Sb in the solution is reduced to 20.2–21.5 μg·L$^{-1,}$ as illustrated in Fig. 8(b). This result highlights the material's persistence in cyclic applications. More importantly, the intrinsically eco-friendly character avoids second contamination after disposal, making it a sustainable alternative to conventional treatments.

3.5. Effect of competing ions on the adsorption of Sb by Fe(0)-CS

Considering the complexity of the aqueous environment in practical applications, the Fe(0)-CS adaptability towards environmental

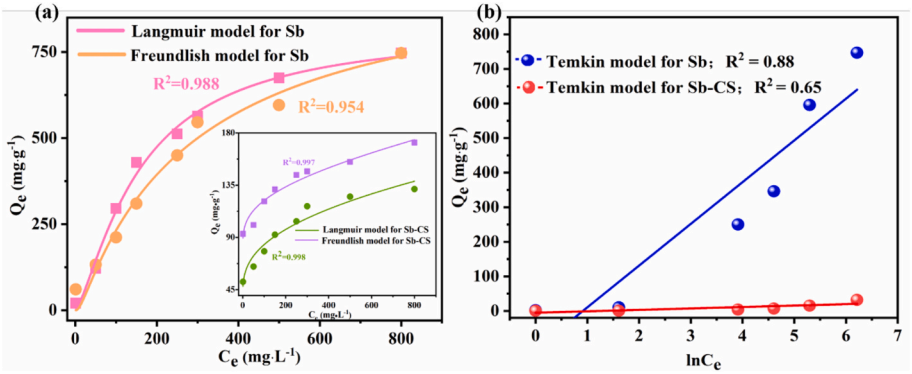


Fig. 6. Isotherms showing the adsorption of Sb ions onto pristine CS and Fe(0)-CS and fitting results with Langmuir, Freundlich, and Temkin isotherm models.

Table 2
Fitting parameters of Freundlich, Langmuir, and Temkin models.

	Langmuir			Freundlich				Temkin		
	Q_m ($mg·g^{-1}$)	K_L ($L·mg^{-1}$)	R^2	1/n	K_F $L·mg^{-1}$	Q_m/$mg·g^{-1}$ ($mg·g^{-1}$)	R^2	K_T/ $L·g^{-1}$	b	R^2
Sb-Fe(0)-CS	903.1	$3.2•10^{-3}$	0.988	0.49	36.63	769.7	0.954	0.4	20.5	0.88
Sb-CS	76.2	4.908	0.98	0.884	0.13	31.6	0.997	0.28	597.3	0.65

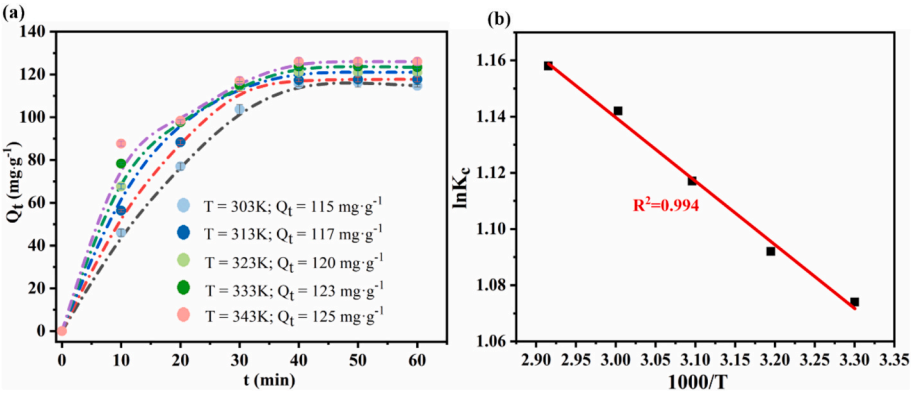


Fig. 7. The fitted curve of lnK_c versus 1000/T for the estimation of thermodynamic parameters for adsorption of Fe(0)-CS for Sb.

Table 3
Thermodynamic adsorption parameters for Sb adsorption onto Fe(0)-CS.

T(K)	Q_e ($mg·g^{-1}$)	K_c	ΔG ($kJ·mol^{-1}$)	ΔH ($kJ·mol^{-1}$)	ΔS ($J·mol^{-1}·K^{-1}$)
303	115	3.762	−3.3	95.9	42.8
313	117	4.383	−3.8		
323	120	4.784	−4.1		
333	123	5.353	−4.6		
343	125	5.925	−5.1		

interference was examined by adding competing cations Co^{2+}, Ni^{2+}, Cu^{2+}, As^{3+}, $Sr^{+,}$ and Cd^{2+} with comparable concentrations into tap water. The adsorption capacity Q_e was calculated, and the kinetics for each ion were depicted in Fig. 9. The initial C_0 and final concentration C_e for all ions after adsorption were compared in Table 4. The adsorption is very fast and completed even in the presence of competing ions, and a capacity of 159.2 $mg·g^{-1}$ resulted that overlapped the optimal performances discussed above. The adsorption capacities for all competing ions are significantly low, with merely 13.98–29.33 $mg·g^{-1}$. The equal portion distributions (K_d=C_0/C_e) of each competing ion are thus calculated and summarized in Table 4. The adsorbent constant values were compared, and the relative distribution constant ratio defined by $K_{Sb/M}$ ($K_{Sb/M} = k_{Sb}/k_M$, k_M: constant values of the competing cations, M = Co^{2+}, Ni^{2+}, Cu^{2+}, As^{3+}, Sr^{+}, and Cd^{2+}) all exceeded 214.0 [58], and some were even as large as 4547.7. This indicates that the CS-supported Fe(0) material exhibits little impact in its performance in the presence of various common ions [59], highlighting the material's durability in complicated environmental conditions.

3.6. Adsorption mechanisms of Sb by Fe(0)-CS

The removal capacity of antimony is related to the surface and inner core of the adsorbent materials. This is because the outer sphere of the Fe (0) nanoparticles has a very high propensity to be oxidized to form an iron oxides ($Fe^{3+,2+}$) shell [60]. This reaction is inevitable even in the presence of a trace of oxygen but is crucial to shielding the Fe(0) core from further oxidation. The surface iron oxides/hydroxides provide coordination and electrostatic interactions to adsorb charged Sb ions. The Fe(0) species in the core has a strong tendency to $Fe^{3+,2+}$ (Fig. 10a, 709.88 eV vs Fig. 10b, 709.48 eV), converting Sb(V) to Sb(III) via electron transfer through the outer layer [60–61]. Then, we evaluate the fraction evolution before and after the process by calculating each integration in XPS. Half of Fe (0) species on the surface was found to be converted to higher states as illustrated in Fig. 7a (before adsorption) vs 7b (after adsorption). The total Fe(II) species is decreased by 20 %, also.

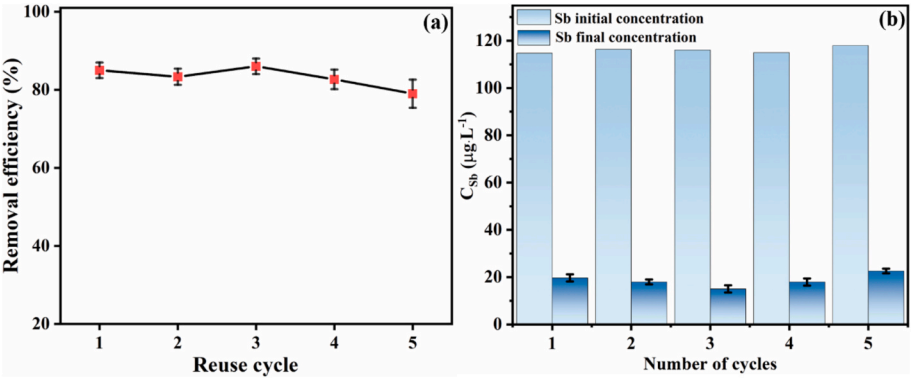


Fig. 8. The regeneration and reuse of Fe(0)-CS: removal efficiency (a) and initial vs residual Sb concentration (b).

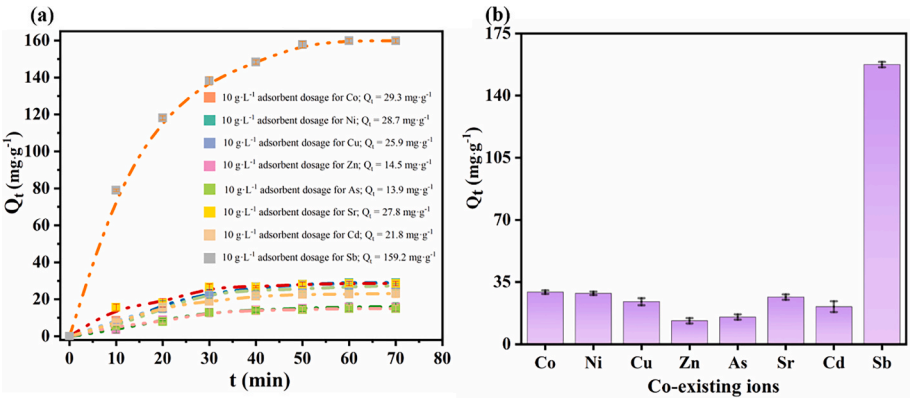


Fig. 9. The interference effect of various cations on the adsorption performances of Fe(0)-CS for Sb.

Table 4
Thermodynamic adsorption parameters for Sb using Fe(0)-CS.

Ion	C_0 (mg·L^{-1})	C_e (mg·L^{-1})	Q_e (mg·g^{-1})	K_d (mg·mg^{-1})	$K_{Sb/Co}$	$K_{Sb/Ni}$	$K_{Sb/Cu}$	$K_{Sb/Zn}$	$K_{Sb/As}$	$K_{Sb/Sr}$	$K_{Sb/Cd}$
Sb	128.04	0.7	159.17	181.9	214.0	219.2	236.2	4547.7	491.6	221.8	336.9
Co	51.1	27.6	29.33	0.8	–	–	–	–	–	–	–
Ni	50.6	27.7	28.67	0.8	–	–	–	–	–	–	–
Cu	47.9	27.1	25.93	0.8	–	–	–	–	–	–	–
Zn	37.3	25.7	14.52	0.04	–	–	–	–	–	–	–
As	38.4	27.3	13.98	0.4	–	–	–	–	–	–	–
Sr	49.5	27.3	27.85	0.8	–	–	–	–	–	–	–
Cd	49.8	32.3	21.85	0.5	–	–	–	–	–	–	–

Accordingly, the fraction of Sb(V) species was increased by 80 % as result.

In our case, the porous CS coverlet, particularly the OH moiety, may alter the Fe(0) interface state and then accelerates both the diffusion kinetics of Sb and surface adsorption during the adsorption, as discussed in Fig. 5c. This interaction can be testified by the changes from free OH (532.5 eV, Fig. 10c) of CS surface before adsorption into a week Sb-OH interaction (532.4 eV, Fig. 10d) after adsorption, and at the same time, the Fe-O shifts from 530.08 eV into 530.28 eV (Fig. 10a) [58,62].

The percentage of Sb before and after the process was calculated based on the integration and noted in Fig. 10e and f, respectively. Sb(III) decreased from 60 % to 50 % and Sb(V) increased 25 % to 45 %. Considering the complexity of the original Sb oxidation states of the aqueous sample used in all experiments, we tested individual pathways of the Sb(III) and Sb(V) during the process by using pure Sb samples. The adsorption experiment initially using the Sb(V) sample was carried out. The majority of species is reduced to Sb(III) (Fig. 10*h*), and the XPS further confirms the formation of Sb_2O_3 [61]. These results offer confirmatory evidence for the reducing role of Fe(0) during the adsorption [62]. An adsorption experiment on pure Sb(III) was also conducted, and the XPS result revealed in Fig. 10g) clearly points out that Sb(III) species are partially oxidized to Sb_2O_5 during the process, presumably due to the presence of oxygen traces. Therefore, both reduction and oxidation reactions are acting during the process in our cases, resulting in Sb(III) and Sb(V) interconversion.

The pH influences the nature of the surface and Sb species based on the mechanism proposed above [63–64]. At pH < 4.0, H^+ ions could bind with surface hydroxyl groups of CS and iron oxide to form OH_2^+ moieties [64–65], providing extra adhesion sites and electrostatic attraction force for anionic $H_2SbO_3^-$ or $Sb(OH)_4^-$ species (H_3SbO_4, pK_a = 2.72). This interaction facilitates reduction of Sb and subsequent precipitate on the CS surface. At pH > 4.0, the performances was influenced [64,66], particularly, the adsorption was declined below 40.0 mg·g^{-1} when the pH is beyond 9.0. This chemisorption can be corroborated by a maximum equilibrium adsorption capacity near 4 from pH dependent-experiment depicted in Fig. 11. The results here provide a comprehensive understanding of this robust adsorption process.

4. Conclusions

Antimony, a toxic metalloid, poses considerable risks to aquatic life and human health due to its persistence and mobility in water bodies. The removal of antimony from water using a zero-valent iron adsorbent embedded in chitosan offers significant environmental benefits. Zero-valent iron nanoparticles supported by porous chitosan materials, Fe (0)-CS, are fabricated and characterized by several measurements. The developed material is a novel adsorbent for removing Sb contaminants in aqueous solutions following a synergistic oxidation and ionic interaction pathway. This eco-friendly material efficiently captures both Sb (III) and Sb(V), is biodegradable and can be reused with minimal performance loss. The presence of well-dispersed nano-Fe(0) among the CS boosts Sb(III) formation and anchoring, and elevates the adsorption capacity up to 175.89 mg_{Sb} g_{Ad}^{-1} or 2240.73 mg_{Sb} g_{Fe}^{-1}. The adsorption follows the well-behaved second-order kinetic and the Langmuir isothermal model. Subsequent recovery of Sb and materials over 80.9 % shows high robustness and reusability of the system after five consecutive adsorption–desorption cycles. The material displayed high resilience to other common interfering cations such as Co^{2+}, Ni^{2+}, Cu^{2+}, As^{3+}, Sr^{+}, and Cd^{2+} competing constant ratios $K_{Sb/M}$ up to 214–4548. The developed doping strategy offers enormous potential for constructing advanced materials for treating metal-polluted water media and other hazardous substances. Its low toxicity and ability to minimize secondary pollution make it a sustainable alternative to conventional treatments. Moreover, using chitosan from biomass waste supports circular economy principles. This approach offers a cost-effective and environmentally friendly solution to addressing heavy metal contamination in aquatic environments.

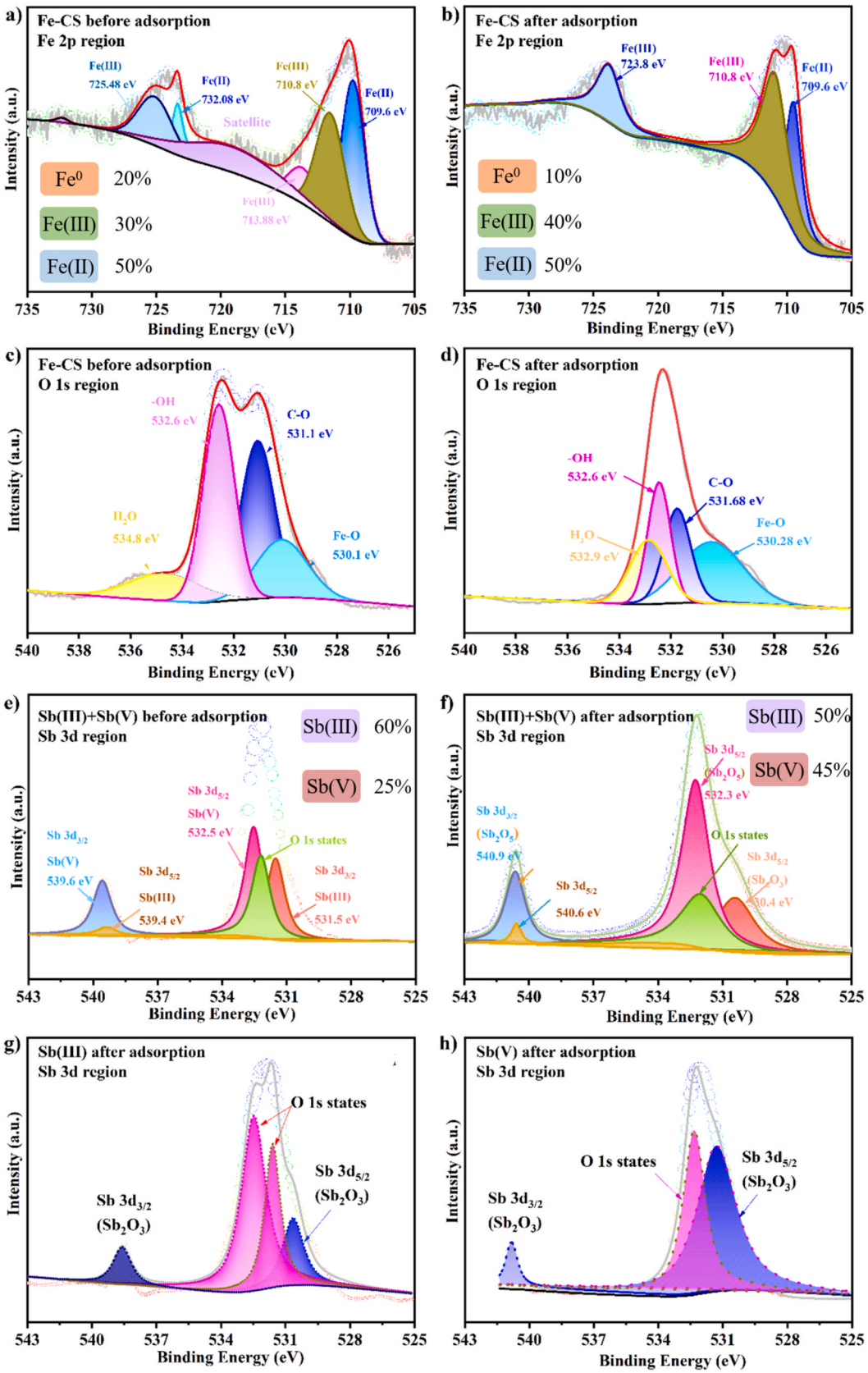


Fig. 10. The XPS analyses for Fe (a, b), O (c, d), Sb(III and V) (e, f) before and after the adsorption, and Sb (III) (g) and Sb(V) (h) after adsorption.

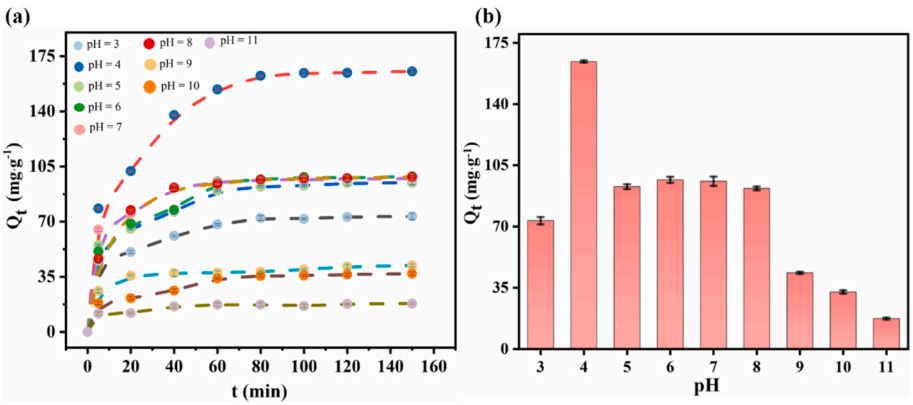


Fig. 11. The effect of pH on adsorption capacity and efficiency of Fe(0)-CS for Sb removal.

CRediT authorship contribution statement

Hongjie Wu: Writing – original draft, Software, Methodology, Investigation, Data curation. **Xiaoyu Jia:** Conceptualization, Resources, Data curation, Writing – original draft, Writing – review & editing, Supervision, Project administration, Funding acquisition. **David Hermann Lamparelli:** Writing – review & editing, Validation, Methodology, Investigation, Formal analysis, Data curation. **Dirong Gong:** Conceptualization, Resources, Data curation, Writing – original draft, Writing – review & editing, Supervision, Project administration, Funding acquisition. **Antonio Buonerba:** Conceptualization, Validation, Formal analysis, Investigation, Data curation, Writing – original draft, Writing – review & editing, Visualization, Supervision, Funding acquisition.

Declaration of competing interest

The authors declare that they have no known competing financial interests or personal relationships that could have appeared to influence the work reported in this paper.

Acknowledgments

Financial support is gratefully from: *i*) the Natural Science Foundation of Zhejiang (Y19B040010) and the Natural Science Foundation of Ningbo (2023J080); *ii*) Ministero dell'Università della Ricerca (Ministry of University and Research, MUR, Rome, Italy) for the grant: PRIN2022 *"Finanziato dall'Unione europea-Next Generation EU, Missione 4, Componente 1-CUP: D53D23017260001"*; *iii*) Università degli Studi di Salerno (University of Salerno, Fisciano, SA, Italy) for the grants: FARB ORSA224812, FARB ORSA239513, and FARB ORSA247407.

Appendix A. Supplementary data

Supplementary data to this article can be found online at https://doi.org/10.1016/j.seppur.2025.133807.

Data availability

Data will be made available on request.

References

[1] C. Yao, F. Che, X. Jiang, Z. Wu, J. Chen, K. Wang, Study on antimony mobility in a contaminated shallow lake sediment using the diffusive gradients in thin films technique, Chemosphere 267 (2021) 128913.
[2] A. Azari, M. Abtahi, R. Saeedi, A.R. Yari, M.H. Vaziri, G. Mohammadi, Integrated ultrasound-assisted magnetic solid-phase extraction for efficient determination and pre-concentration of polycyclic aromatic hydrocarbons from high-consumption soft drinks and non-alcoholic beers in Iran, J. Sep. Sci. 45 (2022) 3139–3149.
[3] H. Kamani, M. Ghayebzadeh, A. Azari, F. Ganji, Characteristics of microplastics in a hospital wastewater treatment plant effluent and hazard risk assessment, Environ. Processes 11 (2024) 1–5.
[4] H. Kamani, L. Mohammadi, A. Azari, S.D. Ashrafi, F. Heydari, F. Ganji, S. M. Mousavi, Application of thymus species as natural coagulant for elimination of turbidity of water and its comparison with the conventional coagulant, J. Environ. Health Sustain. Develop. 9 (2024) 2341–2353.
[5] H. Kamani, M. Hosseinzehi, M. Ghayebzadeh, A. Azari, S.D. Ashrafi, H. Abdipour, Degradation of reactive red 198 dye from aqueous solutions by combined technology advanced sonofenton with zero valent iron: characteristics/effect of parameters/kinetic studies, Heliyon 10 (2024) 1.
[6] H. Lu, W. Zhang, L. Tao, F. Liu, J. Zhang, Enhanced removal of antimony by acid birnessite with doped iron ions: companied by the structural transformation, Chemosphere 226 (2019) 834–840.
[7] L. Wang, J. Wang, Z. Wang, C. He, W. Lyu, W. Yan, L. Yang, Enhanced antimonate (Sb(V)) removal from aqueous solution by La-doped magnetic biochars, Chem. Eng. J. 354 (2018) 623–632.
[8] A. Azari, H. Kamani, M. Sarkhosh, N. Vatankhah, M. Yousefi, Mahmoudi-Moghaddam, Nectarine core-derived magnetite biochar for ultrasound-assisted preconcentration of polycyclic aromatic hydrocarbons (PAHs) in tomato paste: a cost-effective and sustainable approach, Food Chem. 24 (2024) 101810.
[9] H. Abdipour, A. Azari, H. Kamani, K. Pirasteh, F.K. Mostafapour, S. Rayegnnakhost, Human health risk assessment for fluoride and nitrate contamination in drinking water of municipal and rural areas of Zahedan, Iran, Appl. Water Sci. 15 (2025) 3–47.
[10] X. He, X. Min, X. Luo, Efficient removal of antimony(III, V) from contaminated water by amino modification of a zirconium metal–organic framework with mechanism study, J. Chem. Eng. Data 62 (2017) 1519–1529.
[11] J.P. Zou, H.L. Liu, J. Luo, Q.J. Xing, H.M. Du, X.H. Jiang, X.B. Luo, S.L. Luo, S. L. Suib, Three-dimensional reduced graphene oxide coupled with Mn_3O_4 for highly efficient removal of Sb(III) and Sb(V) from water, ACS Appl. Mater. Interfaces 8 (2016) 18140–18149.
[12] M. Arnold, P. Kangas, A. Mäkinen, E. Lakay, N. Isomäki, G. Lavén, M. Gericke, P. Pajuniemi, T. Kaartinen, L. Wendling, Mine water as a resource: selective removal and recovery of trace antimony from mine-impacted water, Mine Water Environ. 38 (2019) 431–446.
[13] M. Li, Y. Liu, C. Shen, F. Li, C.C. Wang, M. Huang, B. Yang, Z. Wang, J. Yang, W. Sand, One-step Sb(III) decontamination using a bifunctional photoelectrochemical filter, J. Hazard. Mater. 389 (2020) 121840.
[14] H. Zhang, X. Liu, Y. Jiang, L. Gao, L. Yu, N. Lin, Y. He, C.T. Liu, Direct separation of arsenic and antimony oxides by high-temperature filtration with porous FeAl intermetallic, J. Hazard. Mater. 338 (2017) 364–371.
[15] J. Zeng, P. Qi, J. Shi, T. Pichler, F. Wang, Y. Wang, K. Sui, Chitosan functionalized iron nanosheet for enhanced removal of As(III) and Sb(III): synergistic effect and mechanism, Chem. Eng. J. 382 (2020) 122999.
[16] R.J. Deng, C.S. Ren, B.Z. Hou, A.S. Hursthouse, The potential for the treatment of antimony-containing wastewater by iron-based adsorbents, Water 9 (2017) 10–794.
[17] K. Yang, J. Zhou, Z. Lou, X. Zhou, Y. Liu, Y. Li, S.A. Baig, X. Xu, Removal of Sb(V) from aqueous solutions using Fe-Mn binary oxides: the influence of iron oxides forms and the role of manganese oxides, Chem. Eng. J. 354 (2018) 577–588.
[18] J. Luo, X. Luo, J. Crittenden, J. Qu, Y. Bai, Y. Peng, J. Li, Removal of antimonite (Sb (III)) and antimonate (Sb(V)) from aqueous solution using carbon nanofibers that are decorated with zirconium oxide (ZrO_2), Environ. Sci. Tech. 49 (2015) 11115–11124.
[19] P. Qi, R. Luo, T. Pichler, J. Zeng, Y. Wang, Y. Fan, K. Sui, Development of a magnetic core-shell Fe_3O_4@TA@UiO-66 microsphere for removal of arsenic(III) and antimony(III) from aqueous solution, J. Hazard. Mater. 378 (2019) 120721.
[20] C. Zhang, H. Jiang, Y. Deng, A. Wang, Adsorption performance of antimony by modified iron powder, RSC Adv. 9 (2019) 31645–31653.
[21] V.K. Mittal, S. Bera, S.V. Narasimhan, S. Velmurugan, Adsorption behavior of antimony(III) oxyanions on magnetite surface in aqueous organic acid environment, Appl. Surf. Sci. 266 (2013) 272–279.

[22] G. Xue, Q. Wang, Y. Qian, P. Gao, Y. Su, Z. Liu, H. Chen, X. Li, J. Chen, Simultaneous removal of aniline, antimony and chromium by ZVI coupled with H_2O_2: implication for textile wastewater treatment, J. Hazard. Mater. 368 (2019) 840–848.
[23] C. Dai, Z. Zhou, X. Zhou, Y. Zhang, Removal of Sb(III) and Sb(V) from aqueous solutions using nZVI, Water Air Soil Pollut. 225 (2013) 1799.
[24] M. Moradi, O.B. Naeej, A. Azari, A.M. Bandpei, A.J. Jafari, A. Esrafili, R. R. Kalantary, A comparative study of nitrate removal from aqueous solutions using zeolite, nZVI–zeolite, nZVI and iron powder adsorbents, Desalin. Water Treat. 74 (2017) 278–288.
[25] C. Xu, B. Zhang, L. Zhu, S. Lin, X. Sun, Z. Jiang, P.G. Tratnyek, Sequestration of antimonite by zerovalent iron: using weak magnetic field effects to enhance performance and characterize reaction mechanisms, Environ. Sci. Tech. 50 (2016) 1483–1491.
[26] U. Tyagi, Sustainable and low-cost biomass derived adsorbents for the removal of toxic contaminants from wastewater: approaches and future perspective, Waste Manage. Bull. 2 (2024) 308–325.
[27] I. Anastopoulos, D.A. Giannakoudakis, Z. Frontistis, A.A. Zorpas, I. Pashalidis, K. Triantafyllidis, Biomass-derived adsorbents: universal database development for their synthesis and remediation efficiency as a necessary step to move from laboratory-to pilot-scale applications, Curr. Opin. Green Sustain. Chem. 47 (2024) 100902.
[28] A.A. Markeb, J. Moral-Vico, A. Sánchez, X. Font, Novel nanocomposite synthesis of carboxymethyl cellulose coated to zero-valent iron supported on chitosan for simultaneous removal of heavy metals and pesticides in water: Performance and mechanism, Results Chem. 13 (2025) 102041.
[29] Q. Zhang, D. Zhao, S. Feng, Y. Wang, A. Alsaedi, T. Hayat, C. Chen, Synthesis of nanoscale zero-valent iron loaded chitosan for synergistically enhanced removal of U(VI) based on adsorption and reduction, J. Colloid Interface Sci. 552 (2019) 735–743.
[30] Y. Yang, Y. Xu, D. Zhong, Q. Qiao, H. Zeng, Zr^{4+}-modified chitosan coated nZVI enhance the removal of Cr(VI) by adsorption-reduction interaction, J. Environ. Chem. Eng. 125 (2024) 113315.
[31] H. Bessaies, S. Iftekhar, M.B. Asif, J. Kheriji, C. Necibi, M. Sillanpaa, B. Hamrouni, Characterization and physicochemical aspects of novel cellulose-based layered double hydroxide nanocomposite for removal of antimony and fluoride from aqueous solution, J. Environ. Sci. 102 (2021) 301–315.
[32] A. Hassan, N.M. Sorour, A. El-Baz, Y. Shetaia, Simple synthesis of bacterial cellulose/magnetite nanoparticles composite for the removal of antimony from aqueous solution, Int. J. Environ. Sci. Technol. 16 (2018) 1433–1448.
[33] B. Lapo, H. Demey, T. Carchi, A.M. Sastre, Antimony removal from water by a chitosan-Iron (III) [ChiFer (III)] biocomposite, Polymers 11 (2019) 2–351.
[34] S. Li, X. Hu, J. Zhou, S. Zheng, Q. Ma, H. Fu, W.X. Zhang, Z. Deng, Biomass-derived cellulose nanocrystals modified nZVI for enhanced tetrabromobisphenol A (TBBPA) removal, Int. J. Biol. Macromol. 268 (2024) 131625.
[35] T. Parandhaman, N. Pentela, B. Ramalingam, D. Samanta, S.K. Das, Metal nanoparticle loaded magnetic-chitosan microsphere: water dispersible and easily separable hybrid metal nano-biomaterial for catalytic applications, ACS Sustain. Chem. Eng. 5 (2017) 489–501.
[36] M. Hasanzadeh, Z. Ghaedrahmat, N. Kayedi, N.J.H. Fard, A. Azari, M. Afsharizadeh, Persulfate-assisted heterogeneous photocatalytic degradation of furfural from aqueous solutions using TiO_2–ZnO/biochar composite, Heliyon 9 (2023) 11.
[37] D.W. Cho, B.H. Jeon, C.M. Chon, Y. Kim, F.W. Schwartz, E.S. Lee, H. Song, A novel chitosan/clay/magnetite composite for adsorption of Cu(II) and As(V), Chem. Eng. J. 200 (2012) 654–662.
[38] K.C.M. Kwok, L.F. Koong, T.A. Ansari, G. McKay, Adsorption/desorption of arsenite and arsenate on chitosan and nanochitosan, Environ. Sci. Pollut. Res. 25 (2018) 14734–14742.
[39] J.M. Neto, C.R. Bellato, D. Silva, Iron oxide/carbon nanotubes/chitosan magnetic composite film for chromium species removal, Chemosphere 218 (2019) 391–401.
[40] L.R. Martins, L.C. Soares, L.V.A. Gurgel, L.F. Gil, Use of a new zwitterionic cellulose derivative for removal of crystal violet and orange II from aqueous solutions, J. Hazard. Mater. 40 (2022) 127401.
[41] M. Gao, W. Liu, X. Wang, Y. Li, P. Zhou, L. Shi, B. Ye, R.A. Dahlgren, X. Wang, Hydrogen-bonding-induced efficient dispersive solid phase extraction of bisphenols and their derivatives in environmental waters using surface amino-functionalized MIL-101(Fe), Microchem. J. 145 (2019) 1151–1161.
[42] S. Rangwani, A.J. Howarth, M.R. DeStefano, C.D. Malliakas, A.E. Platero-Prats, K. W. Chapman, O.K. Farha, Adsorptive removal of Sb(V) from water using a mesoporous Zr-based metal-organic framework, Polyhedron 151 (2018) 338–343.
[43] G. Autie-Castro, M.A. Autie, E. Rodriguez-Castellon, C. Aguirre, E. Reguera, Cu-BTC and Fe-BTC metal-organic frameworks: role of the materials structural features on their performance for volatile hydrocarbons separation, Colloids Surf. A 481 (2015) 351–357.
[44] S. Hamzeh, H. Mahmoudi-Moghaddam, S. Zinatloo-Ajabshir, M. Amiri, A. Azari, Simple fabrication of mesoporous praseodymium cerate via an eco-friendly route for development of carbendazim electrochemical sensor, J. Electrochem. Soc. 171 (2024) 3.
[45] F. Gharibzadeh, R.R. Kalantary, A. Esrafili, M. Ravanipour, A. Azari, Desorption kinetics and isotherms of phenanthrene from contaminated soil, J. Environ. Health Sci. Eng. 17 (2019) 171–181.
[46] H. Kamani, M. Baniasadi, H. Abdipour, L. Mohammadi, S. Rayegannakhost, H. Moein, A. Azari, Health risk assessment of BTEX compounds (benzene, toluene, ethylbenzene and xylene) in different indoor air using Monte Carlo simulation in zahedan city, Iran, Heliyon 9 (2023) 1.
[47] X. He, X. Min, T. Peng, Y. Ke, F. Zhao, M. Sillanpaa, Y. Wang, Enhanced adsorption of antimonate by ball-milled microscale zero valent iron/pyrite composite: adsorption properties and mechanism insight, Environ. Sci. Pollut. Res. 27 (2020) 16484–16495.
[48] B. Dousova, M. Lhotka, J. Filip, D. Kolousek, Removal of arsenate and antimonate by acid-treated Fe-rich clays, J. Hazard. Mater. 357 (2018) 440–448.
[49] H. Gu, P. Ju, Q. Liu, G. Sun, J. Liu, R. Chen, J. Yu, J. Zhu, J. Wang, Constructing an Amino-reinforced amidoxime swelling layer on a Polyacrylonitrile surface for enhanced uranium adsorption from seawater, J. Colloid Interface Sci. 610 (2022) 1015–1026.
[50] K.H. Fan, T.J. Zhang, S.Y. Xiao, H. He, J.S. Yang, Z.Y. Qin, Preparation and adsorption performance of functionalization cellulose-based composite aerogel, Int. J. Biol. Macromol. 211 (2022) 1–14.
[51] B. Shen, Z. Guo, B. Huang, G. Zhang, P. Fei, S. Hu, Preparation of hydrogels based on pectin with different esterification degrees and evaluation of their structure and adsorption properties, Int. J. Biol. Macromol. 202 (2022) 397–406.
[52] M.R. Awual, M.M. Hasan, A. Shahat, M. Naushad, H. Shiwaku, T. Yaita, Investigation of ligand immobilized nano-composite adsorbent for efficient cerium (III) detection and recovery, Chem. Eng. J. 265 (2015) 210–218.
[53] W. Xu, H.J. Wang, R.P. Liu, X. Zhao, J.H. Qu, The mechanism of antimony(III) removal and its reactions on the surfaces of Fe-Mn binary oxide, J. Colloid Interface Sci. 363 (2011) 320–326.
[54] Y.Q. Tan, M. Chen, Y.M. Hao, High efficient removal of Pb(II) by amino-functionalized Fe_3O_4 magnetic nano-particles, Chem. Eng. J. 191 (2012) 104–111.
[55] X. Hu, M. Song, S. Li, Y. Chu, W.X. Zhang, Z. Deng, TEMPO oxidized cellulose nanocrystal (TOCNC) scaffolded nanoscale zero-valent iron (nZVI) for enhanced chromium removal, Chemosphere 343 (2023) 140212.
[56] W. Zhang, J. Ou, B. Wang, H.Y. Wang, Q.L. He, J.Y. Song, H.N. Zhang, M.Y. Tang, L.A. Zhou, Y. Gao, S.Q. Sun, Efficient heavy metal removal from water by alginate-based porous nanocomposite hydrogels: the enhanced removal mechanism and influencing factor insight, J. Hazard. Mater. 418 (2021) 126358.
[57] X. Jia, D. Gong, J. Zhao, H. Ren, J. Wang, X. Zhang, Zwitterion-functionalized polymer microspheres as a sorbent for solid phase extraction of trace levels of V (V), Cr (III), As (III), Sn (IV), Sb (III) and Hg (II) prior to their determination by ICP-MS, Microchim. Acta 185 (2018) 1–9.
[58] L. Hao, M. Liu, N. Wang, G. Li, A critical review on arsenic removal from water using iron-based adsorbents, RSC Adv. 8 (2018) 39545–39560.
[59] G. Ungureanu, S. Santos, R. Boaventura, C. Botelho, Arsenic and antimony in water and wastewater: Overview of removal techniques with special reference to latest advances in adsorption, J. Environ. Manage. 151 (2015) 326–342.
[60] Q. Cheng, Q. Li, X. Huang, X. Li, Y. Wang, W. Liu, Z. Lin, The high efficient Sb(III) removal by cauliflower like amorphous nanoscale zero-valent iron (A-nZVI), J. Hazard. Mater. 436 (2022) 129056.
[61] W.J. Guo, Z.Y. Fu, Z.Y. Zhang, H. Wang, S.S. Liu, W.Y. Feng, X.L. Zhao, J.P. Giesy, Synthesis of Fe_3O_4 magnetic nanoparticles coated with cationic surfactants and their applications in Sb(V) removal from water, Sci. Total Environ. 710 (2020) 136302.
[62] N. Wang, N.N. Wang, L. Tan, R. Zhang, Q. Zhao, H.B. Wang, Removal of aqueous As(III) Sb(III) by potassium ferrate (K_2FeO_4): the function of oxidation and flocculation, Sci. Total Environ. 726 (2020).
[63] M. Vithanage, A.U. Rajapaksha, X. Dou, N.S. Bolan, J.E. Yang, Y.S. Ok, Surface complexation modeling and spectroscopic evidence of antimony adsorption on iron-oxide-rich red earth soils, J. Colloid Interface Sci. 406 (2013) 217–224.
[64] Q. Yang, Q. Zhao, S. Ren, Q. Lu, X. Guo, Z. Chen, Fabrication of core-shell Fe_3O_4@MIL-100(Fe) magnetic microspheres for the removal of Cr(VI) in aqueous solution, J. Solid State Chem. 244 (2016) 25–30.
[65] L. Wang, C.L. Wan, Y. Zhang, D.J. Lee, X. Liu, X.F. Chen, J.H. Tay, Mechanism of enhanced Sb(V) removal from aqueous solution using chemically modified aerobic granules, J. Hazard. Mater. 284 (2015) 43–49.
[66] C. Cao, L. Xiao, C. Chen, X. Shi, Q. Cao, L. Gao, In situ preparation of magnetic Fe_3O_4 chitosan nanoparticles via a novel reduction-precipitation method and their application in adsorption of reactive azo dye, Powder Technol. 260 (2014) 90–97.